Experimental Mechanics
DOI 10.1007/s11340-006-9021-9

A Study of Crack–inclusion Interactions and Matrix–inclusion Debonding Using Moiré Interferometry and Finite Element Method

P.C. Savalia · H.V. Tippur

Received: 24 June 2006 / Accepted: 30 October 2006
© Society for Experimental Mechanics 2007

Abstract Failure behavior of composite materials in general and particulate composites in particular is intimately linked to interactions between a matrix crack and a second phase inclusion. In this work, surface deformations are optically mapped in the vicinity of a crack–inclusion pair using moiré interferometry. Edge cracked epoxy beams, each with a symmetrically positioned cylindrical glass inclusion ahead of the tip, are used to simulate a compliant matrix crack interacting with a stiff inclusion. Processes involving microelectronic fabrication techniques are developed for creating linear gratings in the crack–inclusion vicinity. The debond evolution between the inclusion–matrix pair is successfully mapped by recording crack opening displacements under quasi-static loading conditions. The surface deformations are analyzed to study evolution of strain fields due to crack–inclusion interactions. A numerical model based on experimental observations is also developed to simulate debonding of the inclusion from the matrix. An element stiffness deactivation method in conjunction with critical radial stress criterion is successfully demonstrated using finite element method. The proposed methodology is shown to capture the experimentally observed debonding process well.

Keywords Crack–inclusion interaction · Heterogeneous materials · Fracture · Interfacial failure · Moiré interferometry · Finite element analysis

Introduction

To address the needs of demanding service environments, it has become a common practice to engineer materials with more than one phase and exploit beneficial characteristics of individual constituents to achieve the desired overall properties. Fiber reinforced composites, particulate composites, functionally graded materials and syntactic foams are a few such multiphase materials commonly used in practice. Further, development of these materials requires an in depth understanding of the mechanics of failure occurring between the matrix and the filler phases in general and the problem of a matrix crack interacting with a second phase inclusion in particular.

Several investigations of the aforesaid problem have been carried out from both analytical and numerical perspectives since the early study of its kind by Tamate [1]. Using Mushkhelishvili's complex potentials, he studied interaction of a radial matrix crack with a circular inclusion in a uniaxially loaded plate. He showed that a relatively stiff inclusion ahead of a compliant matrix reduces stress intensity factor whereas a compliant inclusion ahead of a stiff matrix crack increases the same. Atkinson [2] investigated the problem of a crack outside a perfectly bonded elastic inclusion under uniaxial and biaxial tensions for different crack lengths and elastic properties of the inclusion and matrix. He solved singular integrals numerically and obtained stress intensity factor variation as a function of the distance between the inclusion and the crack tip. Erdogan et al. [3] investigated interactions between a circular inclusion and an arbitrarily oriented crack using Green's functions. They developed expressions for mode-I and mode-II stress intensity factors in terms of asymptotic values of density functions of integral equations which are given in terms of crack face displacements. Gdoutos [4, 5]

P.C. Savalia (SEM member) · H.V. Tippur (✉, SEM member)
Department of Mechanical Engineering, Auburn University,
Auburn, Al 36849, USA
e-mail: tippuhv@auburn.edu

studied interaction between a crack and a hole or a perfectly bonded inclusion in an elastic medium under uniform tension. He investigated critical values of applied stress for crack extension and initial crack extension angle in both cases and reported that a rigid inclusion increases fracture strength of the plate while the opposite occurs in case of a hole. He also later studied stable crack growth when a crack is oriented along a diameter of the inclusion using strain energy density theory. Hasebe et al. [6] studied stress fields in case of debonding between a rigid circular inclusion from the matrix and a resultant interfacial crack in an infinite plate loaded in uniform tension. They modeled the phenomena as a mixed boundary value problem and reported stress intensities at the debond tip. Patton and Santare [7] investigated interaction of a crack with rigid elliptical inclusion in an infinite medium. They examined the problem using Mushkhelishvili's complex potentials and used them to formulate singular integral equations for crack opening displacement and solved for stress intensity factors numerically. It was observed that for relatively flat elliptical inclusions and radially oriented crack with respect to the inclusion, as the crack orients itself towards the flat side of the inclusion the crack tip stress intensity decreases drastically. Li and Chudnovsky [8, 9] performed energy analysis and examined effects of an elastic inclusion on energy release rate (ERR) for crack extension. They studied variations due to inclusion translation, rotation and expansion with respect to the crack tip and showed that a crack approaching a soft inclusion accelerated while a crack approaching a stiff inclusion slowed down. Boundary Element (BE) methods have been used widely to address crack–inclusion problems. Bush [10] used BE formulation to model matrix crack interacting with single and multiple inclusions and reported crack paths and ERR related to crack initiation and growth. This study showed that a crack approaching a particle is shielded from the far field stresses whereas after it passes the inclusion the crack tip stresses are amplified. It was observed that no substantial crack deflection occurs until the tip is within approximately one radius away although ERR effects are noticeable when the distance between the crack and the stiff inclusion is about five radii. He also modeled a weak interface between an inclusion and a matrix by introducing a flaw between the two and showed that it increases ERR substantially and attracts the crack. Knight et al. [11] studied the effect of introducing an interphase region between the inclusion and matrix on ERR and crack trajectories using the BE technique. They studied the effects of Poisson's ratio of the inclusion and the matrix in the absence of an interphase and observed that as the Poisson's ratio of matrix phase approaches incompressibility limit of 0.5, shielding effect and deflection experienced by the crack reduces. They showed that the Poisson's ratio of the inclusion being higher than that of the matrix results in distinct shielding whereas amplification occurs in the opposite scenario. Interphase thickness was shown to affect the crack behavior depending on relative elastic property mismatch between the three phases. Recently, Kitey et al. [12] and Kitey [13] investigated interaction between a crack and a single inclusion and a cluster-of-inclusions using symmetric Galerkin BE method. They showed that a crack propagating through a particle cluster exhibits different trajectories with respect to cluster orientation whereas the overall energy dissipation remains unaltered. In this 2-D study it was also observed that an increase in the area ratio of inclusions to matrix increases ERR and hence material becomes more fracture resistant.

Although many researchers have contributed analytically and numerically to the problem, strikingly few experimental investigations are found in the literature owing to the obvious experimental complexities. O'Toole and Santare [14] have investigated crack–inclusion interactions experimentally using photoelasticity. They simulated an inclusion by bonding two identical steel inclusions on the opposite faces of a polycarbonate plate ahead of a crack. Influence of elliptical inclusions on an edge crack were studied by calculating stress intensity factors from experimental data and showed toughening effect to be the greatest for an elliptical inclusion when its major axis is normal to the crack plane. Another experimental study of the problem is by Li et al. [15]. They experimentally modeled a perfectly bonded 'second phase' inclusion in a matrix by locally altering the chemical structure by selective UV exposure of a polymer. Under fatigue loading conditions, they experimentally measured crack speed and qualitatively observed fractured surface morphology. They reported ERR and crack speed for a crack approaching and penetrating a softer inclusion and showed that crack interaction with a soft or a stiff inclusion alters crack path significantly.

A perfect bond between a matrix and an inclusion seldom exists in reality due to finite interfacial strength. This results in interfacial debonding between the two which in turn plays a significant role in the overall failure process. Presence of a nearby crack would often aggravate the process as well. Apart from the interfacial bond strength, debonding may depend on material properties of the matrix and the inclusion, the geometry of the crack–inclusion pair and the type of loading. The matrix–inclusion debonding causes redistribution of strains and hence stresses in the vicinity of both the inclusion and the crack. These aspects make it important to study and model mechanical fields in the vicinity of a crack–inclusion pair as debonding evolves. The work presented here primarily addresses experimental and finite element modeling of a quasi-statically loaded crack interacting with a second phase inclusion and the evolution of displacement and strain fields due to the debonding process.

Moiré interferometry is a well-known experimental tool pioneered by Post and his coworkers [16, 17] for studying surface displacement and strain fields. To be able to employ this technique successfully, fabrication of a specimen grating of desired spatial frequency is a key step. In this article, use of microfabrication processes to fabricate square-wave profile (amplitude) gratings for moiré interferometry is presented first. These gratings are then used to reproduce physical gratings on a crack–inclusion specimen. A moiré interferometer is developed for real-time mapping of dominant crack opening displacement components in the vicinity of a crack–inclusion pair under quasi-static mode-I loading conditions. The evolution of debonding of an inclusion while interacting with a matrix crack is mapped using the interferometer. The experimental results are subsequently used to guide finite element modeling of the process.

Experimental Details

In the following, the experimental details are described in four parts: (1) fabrication of master gratings on a silicon wafer, (2) techniques of transferring gratings onto the specimen surface, (3) fabrication of crack–inclusion specimen, (4) development of a two-beam moiré interferometer.

Master Grating Fabrication

Microfabrication techniques based on photolithography are routinely used now-a-days for manufacturing integrated circuits and micro-electro-mechanical systems (MEMS) with submicron size features. These processes are adapted in this work to produce master gratings on a silicon wafer. The steps involved are depicted in Fig. 1 and only major details are provided in the following. Further descriptions of the involved processes can be found in the literature [18]. A silicon wafer of thickness 1 mm and diameter 100 mm was used to fabricate master gratings with a square-wave profile. (The relatively thick wafer used here offers convenience of easy handling of the wafer during grating transfer step, to be described later.) A mask for photolithography was designed (using microelectronics design freeware LASI (Layout Systems for Individuals)) with a regular bar and space pattern of pitch 5.08 μm (spatial frequency of 5,000 cycles/in) and procured from a commercial source. This is a chrome-on-glass mask which has transparent glass spaces and opaque chrome bars that makes a square wave pattern. The spatial frequency selected was based on the available in-house microfabrication capabilities and a reasonably high spatial resolution for the work. All microfabrication processes used here were carried out in a clean room environment. As shown in Fig. 1(a) the polished side of the silicon wafer was first cleaned and degreased with acetone and then with

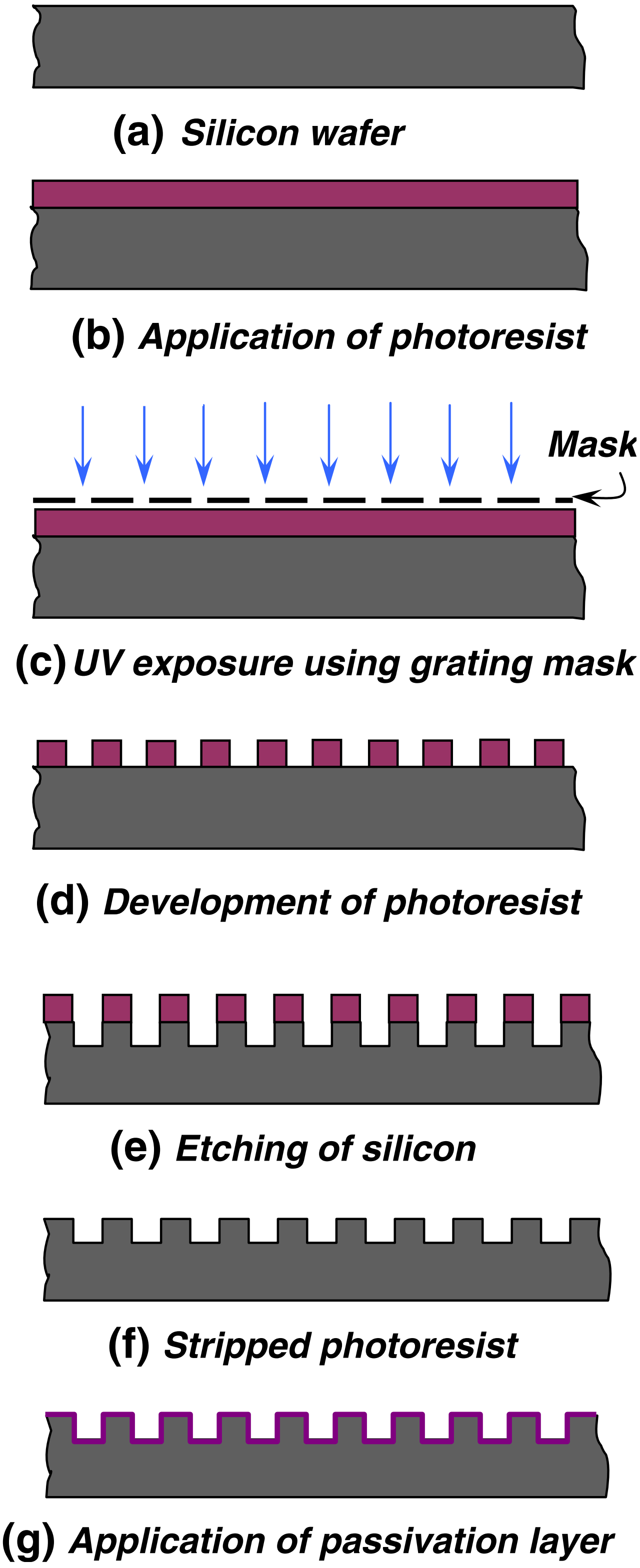
(a) Silicon wafer
(b) Application of photoresist
Mask
(c) UV exposure using grating mask
(d) Development of photoresist
(e) Etching of silicon
(f) Stripped photoresist
(g) Application of passivation layer

Fig. 1 Schematic of the steps involved in the fabrication of silicon wafer master grating

methanol. The wafer was then dried with pressurized nitrogen and hard baked at 120°C for 20 min to ensure that the wafer is moisture free. Next, a positive photoresist AZ 5214 was spin coated on the silicon wafer at 3,500 rpm for about 30 s [Fig. 1(b)] resulting in the photoresist layer of thickness ~1.5 μm. (To enhance adhesion between the photoresist layer and the silicon wafer, adhesion promoting agent namely hexamethayldisilizane (HMDS) was vaporized over the polished wafer surface before spin coating.) The wafer was then soft baked at 120°C for 60 s to let the photoresist cure. Using the chrome-on-glass mask described earlier the photoresist layer was exposed to UV radiation using a mask aligner for pattern transfer [Fig. 1(c)]. The UV radiation changes the property of the exposed photoresist and makes it soluble in a developer while the unexposed areas remain unaffected by the developer. The exposed wafer was then developed and rinsed under flowing deionized water and dried using pressurized nitrogen. This resulted in a silicon wafer with bars of photoresist and bare silicon spaces over it, as shown in Fig. 1(d). Then the wafer was etched [Fig. 1(e)] to a depth of approximately 2.5 μm in the bare spaces between photoresist bars using Inductively Coupled Plasma (ICP) and the photoresist pattern was subsequently stripped [Fig. 1(f)] using oxygen plasma. At the completion of this step a square wave grating profile with bars and spaces was achieved on the silicon wafer. The use of ICP resulted in a very high quality selective etching with straight vertical faces. The wafer was then coated with a very thin passivation layer of fluorocarbon (C_4F_8) which acts as a parting layer in case of direct transfer of gratings from the silicon wafer to the specimen surface [Fig. 1(g)]. A micrograph of the finished silicon wafer gratings is shown in Fig. 4(a) and (b).

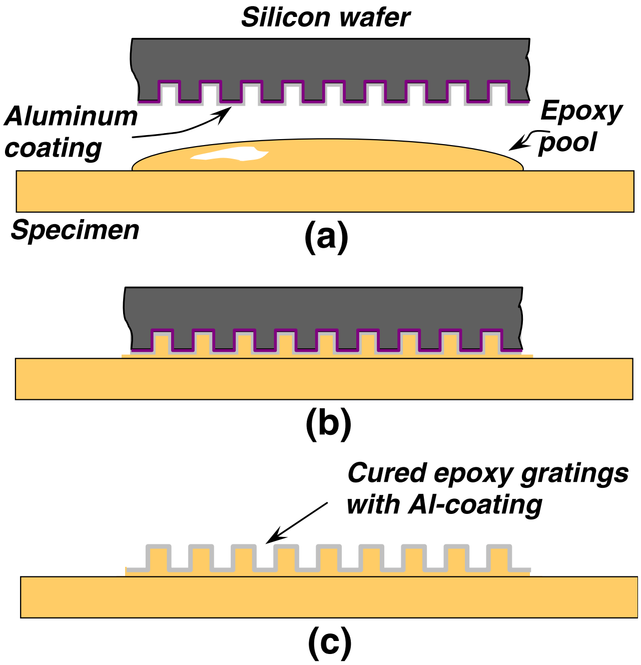

Fig. 2 Schematic of the steps involved in 'direct grating transfer' method (Note: Specimen and gratings are shown in the thickness dimension.)

Grating Transfer Techniques

Two methods were successfully developed to transfer grating pattern fabricated on silicon wafer to a specimen surface: (1) direct grating transfer from silicon master grating, (2) grating transfer using silicone rubber submasters.

The first method is represented schematically in Fig. 2. In this method a thin aluminum layer was vacuum deposited on the silicon wafer after the gratings were prepared as described above. The fluorocarbon passivation layer (C_4F_8) acts as a parting layer between aluminum and silicon. The specimen surface was prepared using no. 220 and then no. 320 grit sand papers before applying a pool of liquid epoxy mixture in the region of interest. The wafer was then gently pressed against the specimen surface over the epoxy[1] pool [Fig. 2(b)]. Excess epoxy was removed and was allowed to cure at room temperature for about 72 h. After epoxy was cured, the silicon wafer was carefully pried off the specimen surface. This resulted in gratings along with an aluminum coating transferred to the specimen surface with a high degree of fidelity [Fig. 2(c)] and reflectivity. (The use of thick (1 mm) wafer was helpful in easy handling of the wafer when being pried off the specimen surface.) The silicon wafer was reused to print gratings on other specimens after redepositing aluminum over it.

In the second method, silicone rubber[2] was used to make submasters or replicas of the master grating pattern. Figure 3 shows various steps involved in fabricating silicone rubber submasters and grating transfer. A cardboard mold was made with its sides parallel and perpendicular to grating lines and fixed to the processed wafer as shown in Fig. 3(a). Two-part silicone rubber was mixed, deaerated, then transferred into the mold and cured at room temperature for about 16 h. The cured rubber submasters were then detached from the silicon wafer. A glob of liquid epoxy was then deposited on the pre-fabricated epoxy specimen in the region of interest [Fig. 3(b)]. The silicone rubber submaster, with its edges aligned with the machined

---

[1] Epoxy used throughout this work is Epo-Thin™ (Product no. 20-1840, 1842, 100 parts resin: 39 parts hardner) from Beuhler Inc., Pennsylvania.

[2] Silicone rubber used is Platsil 73-60 RTV Silicone Rubber manufactured by Polytek Inc., Pennsylvania.

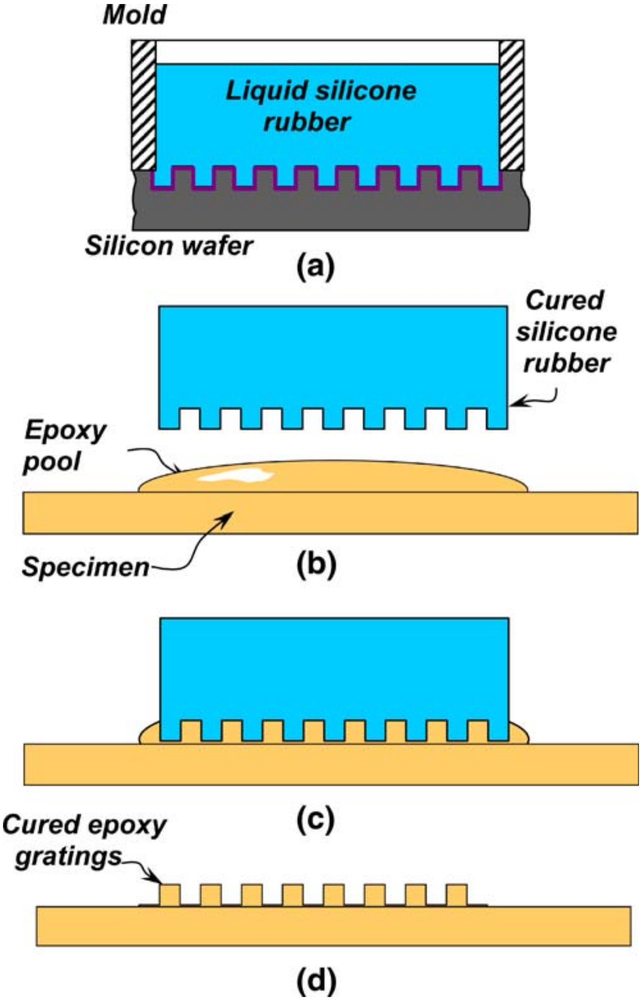

Fig. 3 Schematic of the steps involved in fabricating of silicone rubber submaster (stamp) and transferring grating pattern to specimen surface (Note: Specimen and grating are shown in the thickness dimension.)

specimen edges, was pressed against the specimen surface (prepared with no. 220 and no. 320 grit sand papers) and excess epoxy was squeezed out [Fig 3(c)]. Finally, after the epoxy was cured the rubber mold was detached from specimen with little effort [Fig 3(d)]. This results in high quality amplitude diffraction gratings on the specimen surface. Relatively high diffraction efficiency was obtained from these gratings. (Depositing a reflective metallic film (aluminum, gold, etc.) is optional if higher reflectivity is needed.) This method allowed fabrication of virtually endless numbers of submasters and was tested successfully on both metallic and polymeric substrates. Epoxy gratings transferred using the second method is shown in Fig. 4(d). The cross-section of silicon rubber gratings as viewed under an optical microscope is shown in Fig. 4(b).

Both the methods described above offer alternative approaches to commonly practiced recipes for moiré interferometry. They utilize ubiquitous microelectronics fabrication facilities and do not depend on film based technology and are quite effective. Method-1 does not require preparation of a silicone rubber stamp and hence fewer steps are involved. Further, aluminum film transferred during specimen grating prepration produces good light reflectivity. On the other hand, a thick (approximately 3–4 cm.) silicone rubber stamp of method-2 can be used with relative ease to produce specimen gratings since the possibility of (brittle) silicon wafer breakage during gratings transfer to the specimen exists in method-1. Additionally, for method-1, after transferring the gratings to the specimen the silicon wafer needs to be recoated with aluminum for subsequent use while the silicone stamp in method-2 can be used as is. Thus, both the methods have their own merits based on the needs of an experiment and for the quasi static experiments described in the current study where demand on light intensity is small, method-2 is easier to employ.

Crack–inclusion Specimen Fabrication

Next, specimen preparation for crack–inclusion interaction studies is described. To simulate this problem in a two dimensional setting, epoxy was used as the matrix material and laboratory grade glass was used as the inclusion. The elastic properties of the matrix and the inclusion are listed in Table 1. Pyrex glass rods of diameter 3.8 mm were cut into cylindrical pieces of length 7.1 mm. To enhance the bond strength between glass and epoxy, the glass cylinders were treated with gamma-aminopropyltrimethoxysilane according to manufacturer’s instructions. The glass cylinder was then fixed in a mold of cavity thickness same as the length of the glass cylinder in such a way that the axis of the cylinder was perpendicular to the major dimensions of the mold [see, Fig. 5(a)]. Two part epoxy was then poured into the mold around the inclusion and was cured at room temperature for about 72 h. The cured sample was then machined to the required dimensions and epoxy gratings were printed using one of the methods described previously. It should be noted that, as the gratings and the specimen material are same, shear lag effects are minimum. A notch was then cut into the edge of the specimen using a circular diamond impregnated saw blade (thickness ~300 μm) and then the notch tip was sharpened using a razor blade. Figure 5(b) and (c) depict specimen geometry, dimensions and loading configuration with an illustration of grating direction on them. Here, L is the distance between the crack tip and the center of the inclusion of diameter d. Thus L/d ratio is a nondimensional measure of inclusion proximity to the crack tip and it is 1.31 in this work.

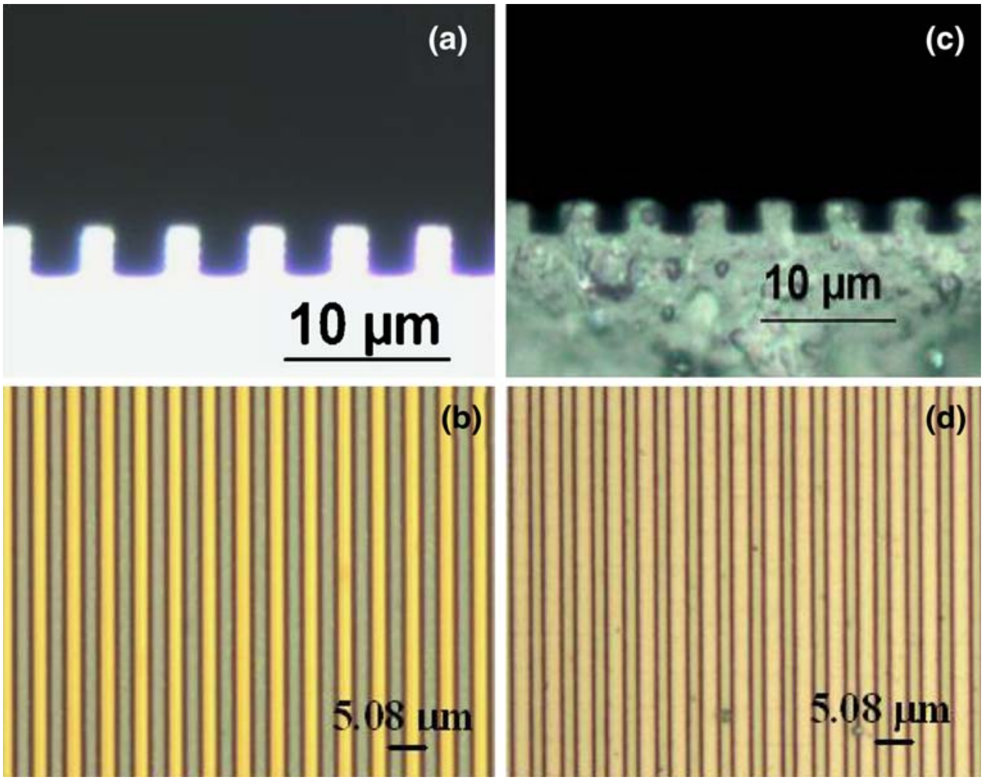

Fig. 4 Optical micrographs of (**a**) Cross-section of etched silicon wafer gratings, (**b**) Front view of etched gratings on silicon wafer, (**c**) Cross-section of silicone rubber submaster gratings, (**d**) Transferred gratings on epoxy beam

Moiré Interferometer—Optical Setup

A moiré interferometer was developed for acquiring full-field displacement contours in the crack tip–inclusion vicinity. Figure 6 is a schematic of the optical setup developed for this work. It includes an 8 mW He-Ne laser, Ronchi grating (R), mirrors (M1, M2, M3 and M4), collimators (C1 and C2), lens (L1) and a CCD camera. The Ronchi grating R is of the same pitch as the specimen grating and helps to achieve the required angle-of-incidence on the specimen easily. The unexpanded laser beam was made to pass through the Ronchi grating (with its principal axis in the horizontal plane in this case) by the mirror M1. The Ronchi grating diffracts the laser beam and produces several diffraction orders in the horizontal plane. The angle α between the diffraction orders is given by,

$$\sin\alpha \simeq \frac{\lambda}{p}, \tag{1}$$

where λ is the wavelength of the laser light and p is the pitch of the grating. For He-Ne laser (λ=633 nm) and grating pitch of 5.08 μm, the value of α is ~7.15°. All but ±1 diffraction orders were blocked by an aperture. These first order diffractions were directed towards mirrors M2 and M3. The reflected laser beams were then directed into beam expanders coupled to collimators C1 and C2, as shown. The collimators were mounted on *x*-*y*-*z* translation stages for fine adjustment. The expanded and collimated laser beams were directed towards the specimen to interfere with each other producing a standing wave of pitch p_v=2.54 μm (10,000 cycles/in) on the specimen surface. These two incident beams, after diffraction by the specimen grating produce ±1 diffractions propagating along the optical axis (shown by dashed line in Fig. 6) towards the camera and carry in-plane deformation information. They are directed into the camera by the mirror M4 and lens L1. The recording system consisting of the lens L1 and a camera back was kept focused on the specimen plane.

Table 1 Elastic properties of matrix and inclusion

	Young's modulus E (GPa)	Poisson's ratio ν
Epoxy	3.5	0.35
Glass	68	0.19

A null field was achieved in no-load condition by making fine adjustments to the collimators. The +1 and −1 orders emerging from the specimen grating and propagating along the optical axis have warped wave fronts (after loading) which interfere and produce moiré fringes. The details of the optical analysis are well known and hence are avoided here for brevity. The fringes represent in-plane displacement components in the principal direction of the specimen grating. In the current investigation crack opening displacements were mapped. The in-plane opening displacement using this setup is given by,

$$v(x,y) = N_y(x,y)p_v, \quad N_y = 0, \pm1, \pm2, \pm3, ..., \tag{2}$$

Fig. 5 Specimen details: (**a**) Specimen preparation, (**b**) Crack tip and inclusion coordinate systems, (**c**) Specimen geometry and loading configuration

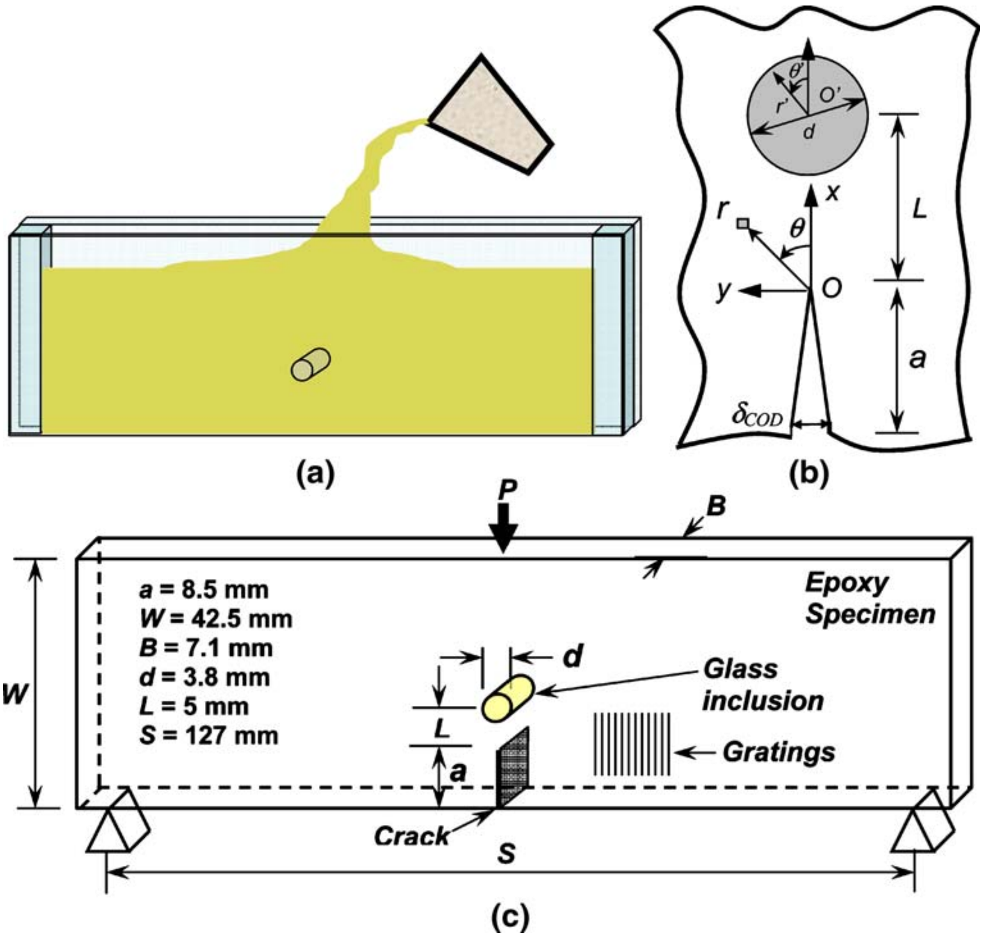

where N_y represents fringe orders and p_v(= 2.54 μm) is the pitch of virtual gratings.

Deformation Field Mapping

The specimen was placed in a loading frame and a null light field was achieved under no-load conditions. A digital CCD camera was interfaced with a computer and was set to time-lapse photography mode to record interferograms at 2 s intervals during the loading phase. A load cell connected to a data logger was also interfaced with the same computer and was configured to log the load history at a rate of 5 samples/s during the event. Both the camera and the data logger were triggered from the computer at the same time as the loading phase was initiated. The specimen was loaded quasi-statically in a three-point bending configuration in the displacement control mode at ~0.04 mm/s. The recording camera was configured to tag each image with the temporal information of the computer clock as the image was dumped into the computer memory. The data logger clock was also synchronized with the computer clock such that loading data and the corresponding time for each data point was recorded. This facilitated establishing load levels at which each image was recorded.

Experimental Results

Materials Characteristics

Epoxy was initially characterized by performing a uniaxial tension test using a 'dog-bone' specimen and the results are shown in Fig. 7. The initial response shows that the epoxy used here is essentially a linear elastic material with a modest nonlinearity before failure. Based on the initial slope of the elastic curve, the elastic modulus is estimated as 3.4±0.1 GPa. The strength of the epoxy used is approximately 63±2 MPa and failure strain is 0.02±0.002.

Bechmark Experiment

Experiments were performed with neat epoxy samples (without any inclusion) in three-point bending configuration and interferograms were recorded at different load levels as described earlier. A typical crack tip fringe pattern for this case is shown in Fig. 7(a)–(c) (1.27 μm/half-fringe). The pattern shows nearly symmetric crack opening displacement contours which is indicative of mode-I loading of the crack tip. An interactive MATLAB™ code was developed to digitize fringes. From the digitized data crack

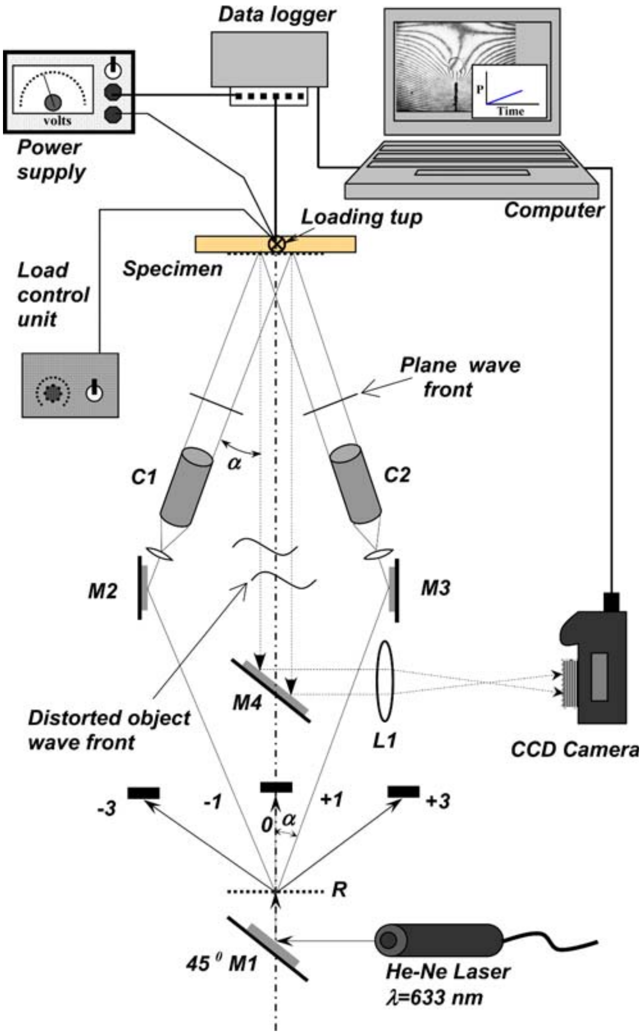

Fig. 6 Schematic of moiré interferometer ($M1$, $M2$, $M3$, $M4$ are mirrors. $C1$, $M2$ are collimators. $L1$ is lens. R is Ronchi grating)

face opening displacements and hence crack mouth opening displacements (CMOD) at the specimen edge for various load levels were determined using equation (2). It should be noted that initial null-field error of one fringe (due to thermal currents and environmental noise) typically exists and affects CMOD data. Another source of error in determining CMOD is specimen edge detection, especially when a dark fringe is hugging the cracked edge. Displacements along (r, θ=180°) were extracted from different interferograms to determine mode-I stress intensity factors (K_I) as a function of the applied load. The method of displacement regression was used for evaluating values of K_I from each interferogram. Using Williams' asymptotic expansion for crack opening displacements, apparent stress intensity factor $(K_\mathrm{I})_\mathrm{app}$ at different crack face locations can be expressed as,

$$(K_\mathrm{I})_\mathrm{app} \approx K_\mathrm{I} + Cr, \tag{3}$$

where,

$$(K_\mathrm{I})_\mathrm{app} = \frac{E\delta\sqrt{2\pi}}{4\sqrt{r}}, \tag{4}$$

and E is Young's modulus, δ is crack opening displacement, r is radial distance measured from the crack-tip and C is the coefficient of the higher order term. Based on equation (3), by plotting K_I as a function of r, one can perform linear regression of $(K_\mathrm{I})_\mathrm{app}$ values to find K_I as [19, 20],

$$K_\mathrm{I} = \lim_{r\to 0}(K_\mathrm{I})_\mathrm{app}. \tag{5}$$

The experimental results of CMOD and K_I thus obtained as a function of load are shown in Fig. 7(e) and (f), respectively. Both variations are essentially linear, as expected for a nominally elastic material such as epoxy used in the current investigation. The last data point corresponds to the onset of fracture. A finite element model of the same problem was also developed using a structural analysis software package ANSYS™ (Version 10.0). Isoparametric quadrilateral elements with midside nodes were used to model the problem in two dimensions under plane stress conditions. The region around the crack-tip was meshed with fine elements to ensure accuracy of the solution. Smallest element size near the crack-tip was approximately 0.005a where a is the crack length. No special elements were used to enforce singularity at the crack-tip. The fracture parameters such as CMOD and mode-I stress intensity factors were extracted from the numerical solution of the developed model. The finite element results for CMOD and mode-I SIF are also shown in Fig. 7(e) and (f), respectively, as solid lines. The numerical data are in very good agreement with the experimental data.

Strain data were also obtained from interferograms along a line (x=3 mm, y) ahead of the crack tip. A central difference scheme was used to extract strain values from the interferograms. Thus obtained strain data was normalized by the maximum tensile strain in an uncracked homogeneous epoxy beam strain,

$$\left(\varepsilon_y\right)_\mathrm{beam} = \frac{3PS}{2EBW^2}, \tag{6}$$

where P is the applied load, S, W, B are specimen dimensions (Fig. 5) and E is the Young's modulus. The corresponding strain plot is shown in Fig. 8 as a function of normalized y (y is normalized by L, the distance between the crack tip and inclusion center in the crack–inclusion specimen, to be described subsequently.) As expected, the strain data is relatively noisy due to numerical differentiation and digitization errors. This is particularly noticeable close to (x, y=0) where optical data tends to be sparse for a mode-I crack tip. Also shown in Fig. 8 is the strain variation obtained from the finite element model along the same line showing good agreement in the overall strain variation trends as well as magnitudes.

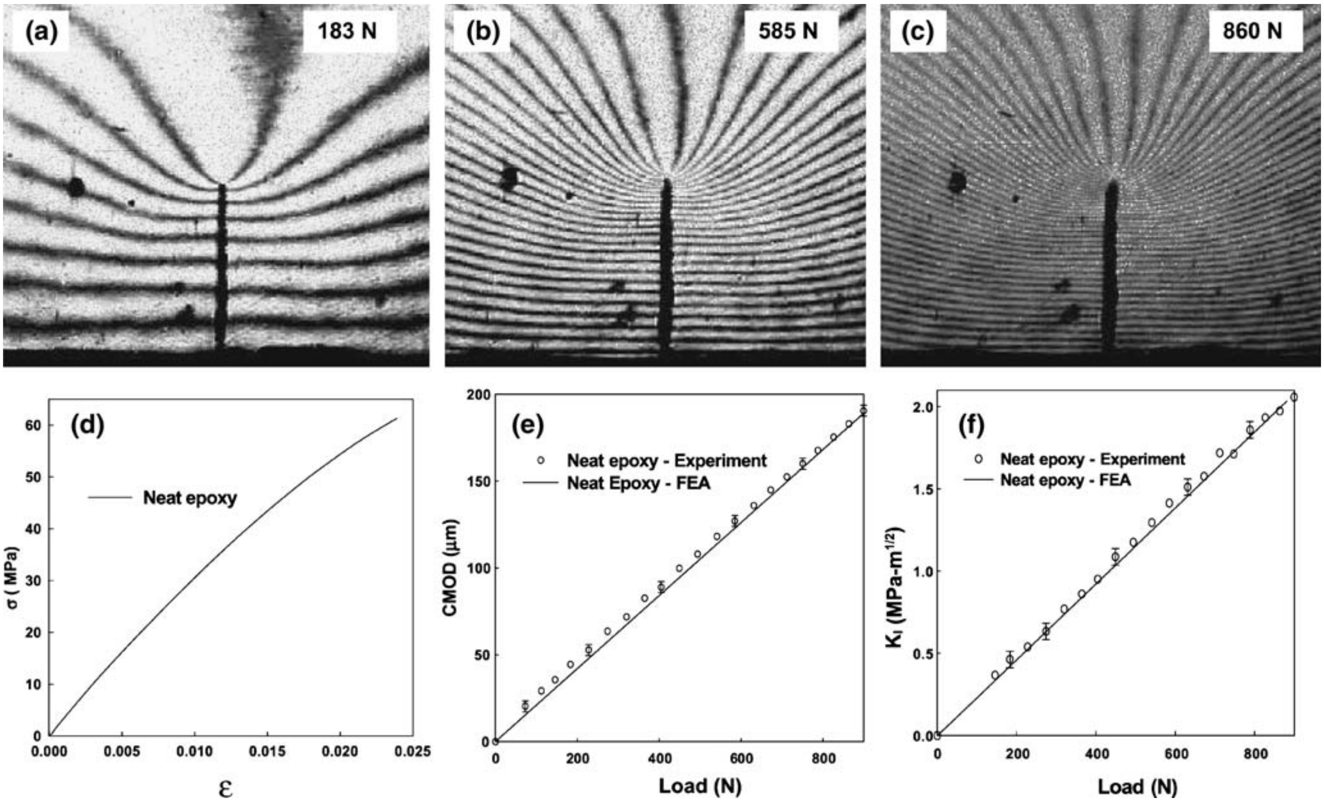

Fig. 7 Results from benchmark study: (**a**–**c**) Moiré interferograms near the crack tip for neat epoxy specimen. (**d**) Stress-strain response for neat epoxy. (**e**) Variation of CMOD with load. (**f**) Variation of mode-I SIF with load (The error bars in (**e**) are based on a one fringe uncertainty in achieving null-field and half-fringe uncertainly in detecting the specimen edge behind the crack tip. The uncertainties in (**f**) associated with K_I evaluation are due to fringe center digitization and crack tip location)

Interaction Between Crack and Inclusion

Next, crack opening displacements were mapped in crack–inclusion specimens described earlier. Figure 5(b) shows the coordinate systems considered. Four selected interferograms at different loads from a typical experiment are shown in Fig. 9. The first two interferograms are for load levels before the inclusion debonds from the matrix and the last two are for after debonding occurs. The interferograms are symmetric near the crack tip and suggests dominant mode-I conditions. Evidently, fringes around the inclusion become discontinuous once debonding occurs. This results in redistribution of strains. The fringes observed within the inclusion are parallel to each other and are equally spaced indicating rigid rotation of the inclusion after debonding, possibly due to incomplete debonding between the matrix and the inclusion. Also, it should be noted that fringes around the inclusion become asymmetric after debonding, likely due to debond path selection around the inclusion as a result of local inhomogeneities. As described previously, CMOD were calculated by counting the number of fringes around the crack up to the edge of the specimen. The CMOD values for an inclusion diameter d=3.8 mm and L/d ratio of 1.31 are shown in Fig. 10(a). In the graph, CMOD shows a noticeable jump when inclusion debonds from the matrix. The values of CMOD for a crack–inclusion specimen are lower before debonding and higher after debonding relative to those for neat epoxy specimen. The effect of debonding on crack mouth compliance, d(CMOD)/dP, of the specimen can be readily visualized in Fig. 10(b). The compliance of the specimen remained almost constant and somewhat lower than the one for neat

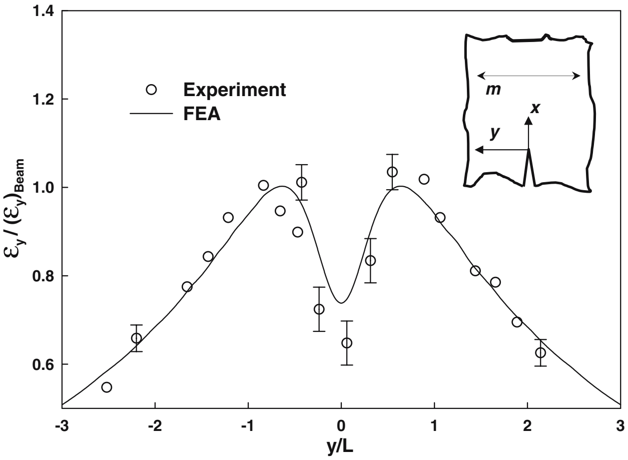

Fig. 8 Comparison of strain distribution in neat epoxy sample along line x~3 mm (L=5 mm, and indicated by m) from moiré data and finite element analysis

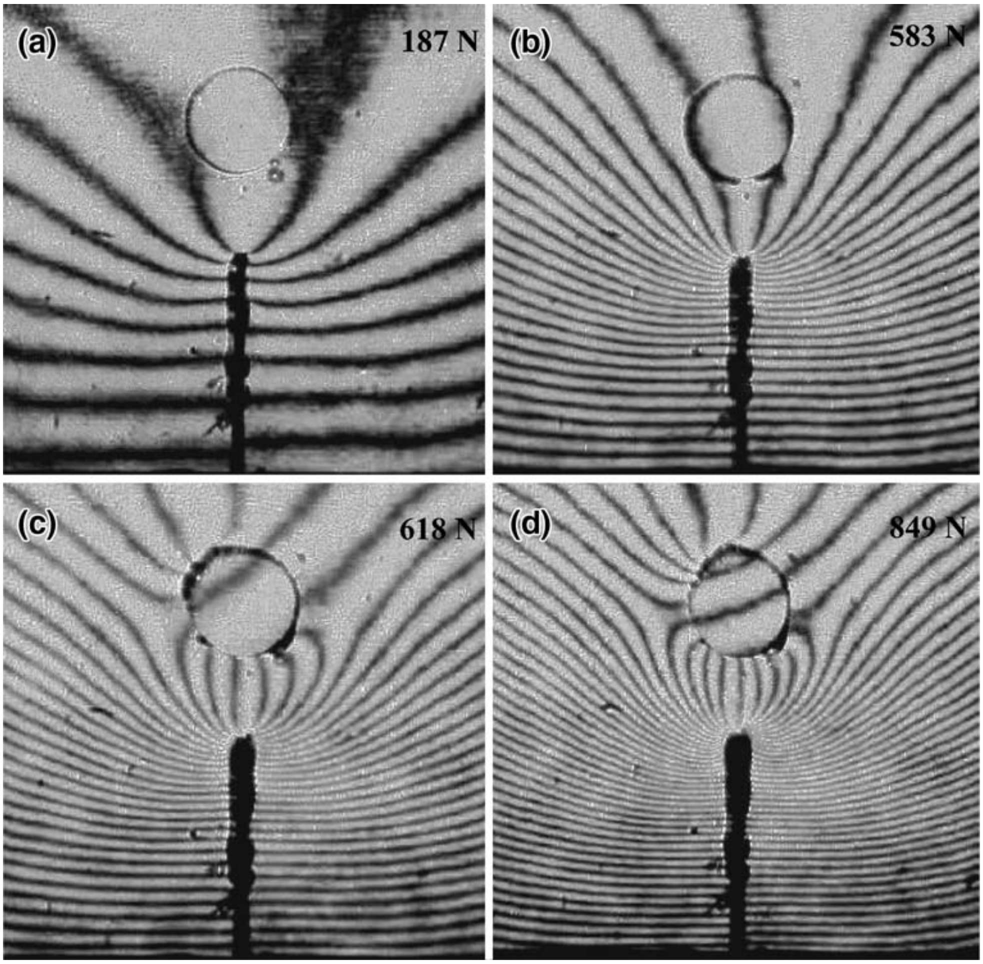

Fig. 9 Selected moiré interferograms for crack–inclusion specimen showing debonding between inclusion and matrix: (**a**), (**b**) Before debonding, (**c**), (**d**) After debonding

epoxy before the onset of debonding. Once debonding occurs, compliance shows a substantial jump. After debonding crack mouth compliance is higher when compared to that for neat epoxy and the ones for pre-debonding regime. For consistency with the benchmark results for neat epoxy shown in Fig. 7, a plot of mode-I stress intensity factors for crack–inclusion specimen is also shown in Fig. 11. The jump in the K_I values when debonding occurs is again evident. The finite element analysis results are also shown in Figs. 10(b) and 11 and will be discussed later on.

The evolution of strain ε_y along a line orthogonal to the crack and at (x=3 mm, y) ahead of the crack tip (between the crack tip and the inclusion and nearly tangential to the inclusion) is shown in Fig. 12. The strain plot shown in Fig. 12(a) corresponds to a load level (530 N) before debonding and Fig. 12(b) corresponds to the one well after debonding (910 N). It can be seen from the plot that there is substantial redistribution of strains ahead of the crack tip following the onset of debonding of the inclusion from the matrix. After debonding occurs, strains close to y=0 increase drastically and attain a peak value. This can also be observed qualitatively in the decreasing fringe spacing near the inclusion–matrix interface and near y=0. The contrast between the homogeneous edge cracked specimen [see Fig. 7(a–c)] and the crack–inclusion specimen (see Fig. 9) in terms of normalized strain can be readily observed. Interestingly, the strain redistribution is a highly localized phenomena and strains remain unaffected beyond $y/L \sim \pm 1$.

Finite Element Modeling

A finite element model was developed in ANSYS™ [21] structural analysis environment for studying crack–inclusion interaction. A three-point-bend geometry (152 mm× 42.5 mm×7.1 mm), same as the one used in the experiments [see, Fig. 5(c)], was modeled. Isoparametric quadrilateral elements (PLANE82) with mid-side nodes were used to create a controlled mesh in the vicinity of the crack-tip and the inclusion. A fine mesh close to the crack tip with an element size of approximately $a/200$ was used. The model also consisted of ‘interfacial/bond layer’ elements all around the inclusion. The thickness of this layer was ~d/100 for an inclusion of diameter d and was estimated from a

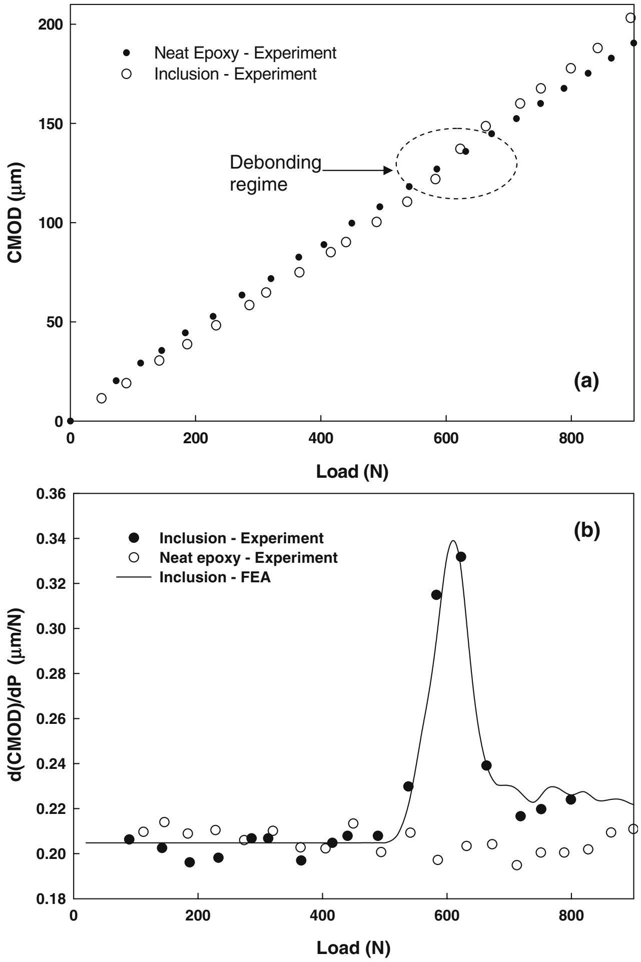

Fig. 10 Comparison of experimentally obtained CMOD variations for crack–inclusion specimen: (**a**) Variation of CMOD with load, (**b**) Variation of crack mouth compliance with applied load

microscopic observation of a silane coated glass cylinder. The total number of elements and nodes in the model were 7,356 and 22,323, respectively. A roller and fixed supports are used as boundary conditions. The finite element mesh used in the simulation is shown in Fig. 13.

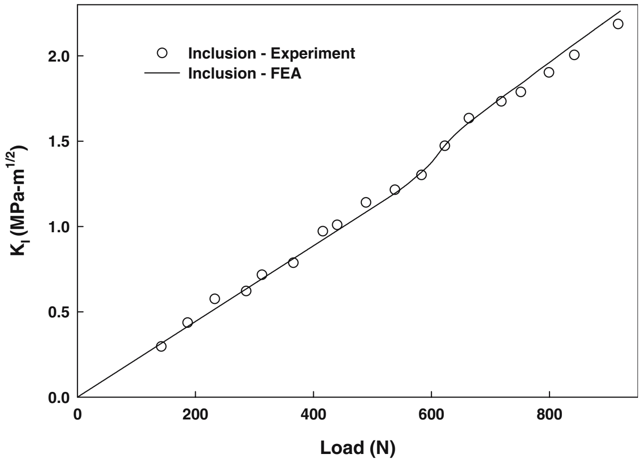

Fig. 11 Variation of mode-I SIF with load for crack–inclusion specimen and comparison with FEA

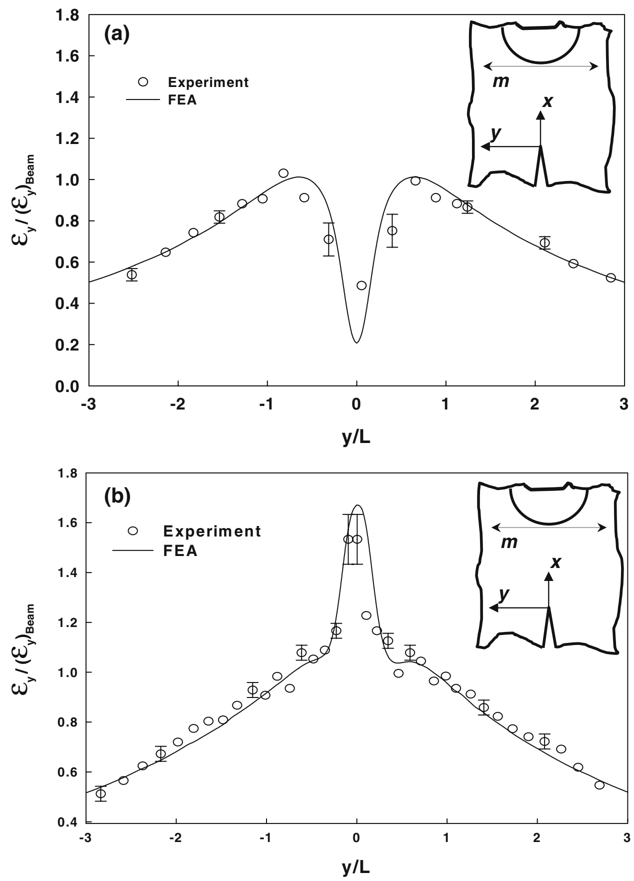

Fig. 12 Strain field evolution along ($x\sim3$ mm, y) (shown by line m) for (**a**) pre-debonding and (**b**) post-debonding stages

A criteria based on the ultimate strength of epoxy was hypothesized to simulate debonding of the inclusion from the matrix and the interfacial elements constituting the bond layer were useful for this. Failure due to radial stress (relative to the origin defined at the inclusion center) was considered for debonding inclusion–matrix interface. It was hypothesized that debonding occurs when radial stress attains a fraction of the ultimate stress of the matrix material. Accordingly, during the loading phase, elements in this bonding layer were monitored. Beyond a predefined value of positive radial stress these bond layer elements were 'killed' (or deactivated) using 'element death' (EKILL) option available in ANSYS.[3] (Some earlier investigations using 'element kill' approach include works

---

[3] It should be noted that cohesive element formulations [24] have become popular in recent years for numerically simulating formation of new surfaces in materials. Several investigators have developed and/or adopted this approach for interfacial failure simulations under static and dynamic loading conditions [25, 26]. If one were to utilize the cohesive element approach, however, interfacial fracture parameters such as fracture energy and critical normal separation distance [27] for the inclusion-matrix system would be necessary. This would involve additional experimentation, beyond the scope of the current work.

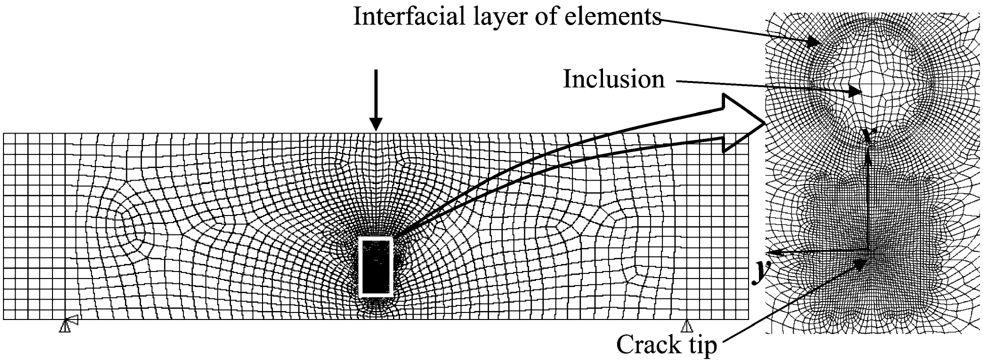

Fig. 13 Finite element mesh used for simulating crack–inclusion interactions in a three-point bend specimen, Inset: Enlarged view of the mesh in the vicinity of crack-tip and inclusion

of Ko et al. [22] and Al-Ostaz and Jasiuk [23]. In the former, the effects of punch-die clearance on the material shearing process in which ductile failure based on effective strain criteria is used to degrade the element stiffness. In the latter, crack growth in a planar porous medium is simulated in perforated sheets by considering elastic strain energy and maximum in-plane normal stress criteria.) A user defined macro using ANSYS Parametric Design Language (APDL) was developed for this purpose. To achieve the desired effect the program does not actually remove the 'killed' elements in the model. Instead, elements meeting a stipulated criterion are deactivated by multiplying their elemental stiffness by a severe reduction factor. In this work a reduction factor of 1×10^{-8} was used. This prevents those deactivated elements from contributing to the overall stiffness of the structure. That is, the respective rows and columns of the stiffness matrix are made negligibly small without replacing them by zeros. The respective loads in the load vector are zeroed out but not removed from the vector. The strain values of all 'killed' elements are set to zero as soon as the elements are deactivated [21]. At the same time, large deformation effects are invoked for these elements to achieve meaningful results.

The criteria proposed for deactivation of an element in the bond layer is,

$$(\sigma_{\mathrm{rr}})_{\mathrm{cr}} = \beta\sigma_{\mathrm{o}}, \tag{7}$$

where $(\sigma_{\mathrm{rr}})_{\mathrm{cr}}$ is the critical value of the radial stress relative to the cylindrical coordinate system with its axis centered at O', σ_{o} is the strength of the matrix material and β is a scalar ($0\leq\beta\leq1$). The value of σ_{o} was used as 63 MPa for epoxy based on the tensile test data shown in Fig. 7(a). Various values of β were considered for simulating inclusion debonding. A plot of CMOD as a function of the applied load for various values of β in equation (7) is shown in Fig. 14. Each plot shows a linear variation of CMOD with load until the onset of debonding. The post-debonding regimes have noticeably different slopes when compared to the pre-debonding regimes. A transition zone in between the two can also be identified. On the same plot, experimentally obtained CMOD values from moiré interferometry are also shown. A value of β=0.14 in equation (7) resulted in a good agreement with experimental observations.[4] A lower or a higher value of β relative to this results in initiation of debonding at lower or higher loads, respectively. Following debonding, all graphs coincide with each other. The CMOD results for FE simulations and experiments are shown in Fig. 14.

Strains ε_y along a line ($x\sim3$ mm, y) near the inclusion–matrix interface from the finite element model is shown in Fig. 12. The normalized strain plots show a behavior similar to the one observed in experiments. The difference between experimental and finite element strain values close to the inclusion–matrix interface is not entirely unexpected considering the fact that experimental asymmetry is unavoidable after the inclusion–matrix debonding. Further, strain differences are due to possible digitization and differentiation errors as noted earlier.

Representative plots of crack opening displacement fields from the finite element analysis in the vicinity of crack–inclusion pair, before and after debonding, are shown in Fig. 15. A qualitative agreement between experimentally recorded opening displacements fields (Fig. 9) and the ones from finite element analysis (Fig. 15) is readily evident. This can be observed from the fringes around the inclusion periphery in the interferograms shown in Fig. 9(c) and (d).[5]

Glass–epoxy Interfacial Strength Measurement

To provide a physical interpretation for the value of β=0.14 in equation (7) that provided good agreement with experimental CMOD variation, nominal interfacial strength

---

[4] A convergence study was carried out to examine the effect of bond layer element size on β value that produced good match with experimental results (not shown here for brevity).

[5] Here, no quantitative agreement in the immediate vicinity of the inclusion is claimed since the displacement field asymmetry is due to one fixed and one frictionless roller support conditions used in the numerical simulation, unlike experimental simulations where both supports were rollers with finite friction.

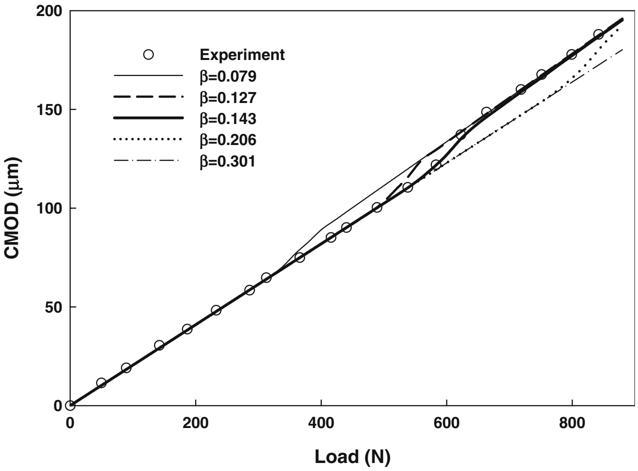

Fig. 14 CMOD variation for various β values [equation (7)] used in finite element simulations and comparison with experimental results (L/d=1.31, d=4 mm)

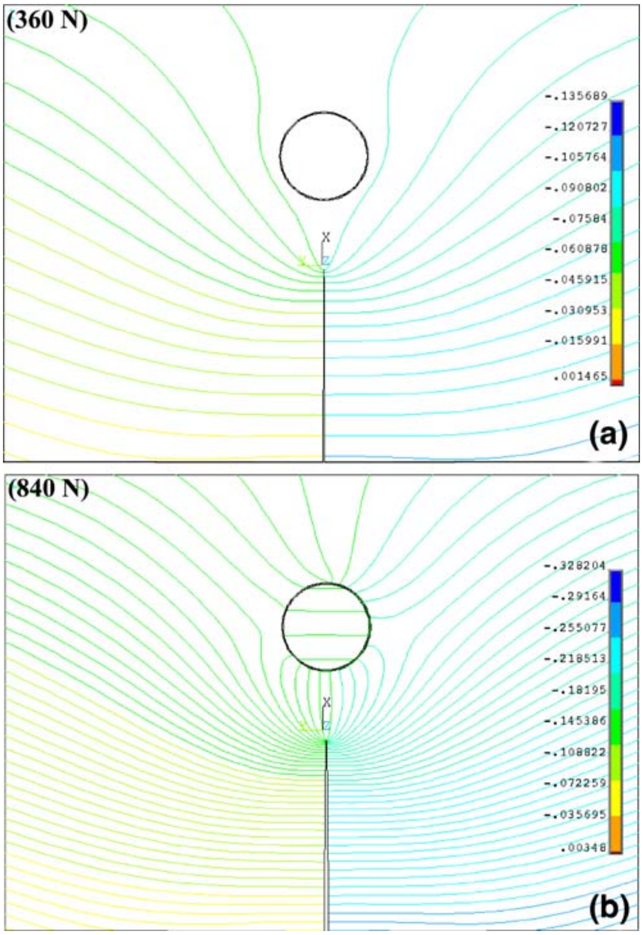

Fig. 15 Crack opening displacement field from finite element analysis showing displacement contours in the crack–inclusion vicinity. (**a**) Before debonding (**b**) After debonding. Contours levels are approximately same as the experimental ones (a=8.5 mm, d=3.8 mm, L/d=1.31, β=0.14)

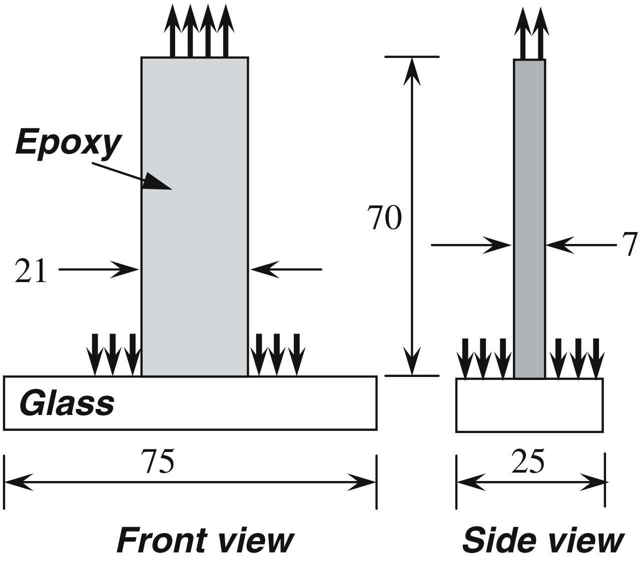

Fig. 16 Schematic of specimens and loading configuration used for estimating glass–epoxy bond strength (Note: All dimensions are in mm.)

between epoxy and glass was measured. This was done using T-shaped tension specimens shown schematically in Fig. 16. The clean surface of a rectangular glass bar (75 mm×25 mm×6.6 mm) that has the surface finish same as that of the glass inclusion was treated with silane and dried at room temperature for 24 h. A silicone rubber mold was prepared to cast epoxy (70 mm×21 mm×7.1 mm) stems on the glass surface. After proper alignment of the mold over the treated glass surface liquid epoxy was poured into the mold and allowed to cure for 72 h at room temperature. Casting epoxy in this way allowed preparing the bond between epoxy and glass in a manner similar to the one that exists between the inclusion and the matrix in crack–inclusion specimens. The specimens were tested in a INSTRON 4465 testing machine and loads at failure of glass-epoxy interface were recorded. Brittle failures of the glass-epoxy interfaces were observed and average failure stresses for several samples tested are reported in Table 2. The average value of the interface strength was estimated as 9.25±1.7 MPa. Interestingly, $(\sigma_{rr})_{cr}$ value in equation (7) that produced good agreement with moiré data is within 5% of the mean interfacial strength between epoxy and glass. This further validates the proposed model used in the FE simulations.

Table 2 Glass–epoxy interfacial failure strength data

Specimen no.	Failure stress (MPa)
1	7.46
2	10.39
3	9.90

Average interfacial failure strength=9.25±1.7 MPa

Conclusions

In this work a stationary crack interacting with a relatively stiff inclusion and the resulting debonding of the inclusion from the matrix were studied experimentally and numerically. Three-point bend (TPB) epoxy specimens, each with an edge crack and a solid cylindrical glass inclusion, were examined. The full-field technique of moiré interferometry was used to map deformations in the crack–inclusion vicinity. The experimental novelty here includes extensive usage of microelectronic fabrication methods for printing specimen gratings using two approaches. A displacement sensitivity of 0.4 fringes/μm was successfully achieved and results were benchmarked using a cracked TPB specimen made of neat epoxy.

Next, deformations near the crack–inclusion vicinity during monotonically increasing load were mapped. Pre- and post-debond deformation fields show localized differences ahead of the crack tip and near the inclusion. The fringe contours clearly show discontinuity at the matrix–inclusion interface and observable asymmetry in displacements around the inclusion due to selective propagation of the debond front. A change in the crack mouth compliance was clearly evident at the onset of debonding. Substantial differences in terms of dominant strains obtained by differentiating optical data were also evident when pre- and post-debond stages were compared.

A finite element model was developed to capture the main experimental observations. This was achieved by implementing a inclusion–matrix debonding criterion based on an interfacial layer of elements attaining a fraction of the ultimate strength of matrix. The debonding process was simulated by degrading the stiffness of interfacial layer of elements. This was accomplished by developing a macro in ANSYS structural analysis environment using an available internal option to degrade element stiffness. The displacement and strain fields were compared with experimental results successfully. A follow up experiment to measure apparent interfacial strength of glass–epoxy suggested that inclusion debonded when radial stress at a location on the interface reached the interfacial strength of the interface. This finite element model thus can be potentially utilized as a tool for studying crack–inclusion interactions such as effects of inclusion–matrix interface strength, elastic mismatch, orientation of inclusion with respect to the crack, to name a few.

Acknowledgments Partial support of the research through grants from National Science Foundation (NSF-CMS-0509060) and Army Research Office (W911NF-04-1-0257) is gratefully acknowledged. Authors also like to thank Mr. Charles Ellis (Alabama Microelectronics Science and Technology Center (AMSTC), Auburn University, Alabama) for assisting in microelectronic fabrication issues and Mr. Madhu Kirugulige for many useful discussions during modeling.

References

1. Tamate O (1968) The effect of a circular inclusion on the stress around a line crack in a sheet under tension. Int J Fract Mech 4:257–266.
2. Atkinson C (1972) The interaction between a crack and an inclusion. Int J Eng Sci 10:127–136.
3. Erdogan F, Gupta GD, Ratwani M (1974) Interaction between a circular inclusion and an arbitrarily oriented crack. J Appl Mech 41:1007–1013.
4. Gduotos EE (1981) Interaction effects between a crack and a circular inclusion. Fibre Sci Technol 15(1):27–40.
5. Gduotos EE (1985) Stable crack growth of a crack interacting with a circular inclusion. Theor Appl Fract Mech 3 (2):141–150.
6. Hasebe N, Okumura M, Nakumura T (1986) Stress-analysis of a debonding and a crack around a circular rigid inclusion. Int J Fract 32(3):169–183.
7. Patton EM, Santare MH (1990) The effect of a rigid elliptical inclusion on a straight crack. Int J Fract 46:71–79.
8. Li R, Chudnovsky A (1993) Energy analysis of crack interaction with an elastic inclusion. Int J Fract 63:247–261.
9. Li R, Chudnovsky A (1994) The stress intensity factor Green's function for a crack interacting with a circular inclusion. Int J Fract 67:169–177.
10. Bush M (1997) The interaction between a crack and a particle cluster. Int J Fract 88:215–232.
11. Knight MG, Wrobel LC, Henshall JL, De Lacerda LA (2002) A study of the interaction between a propagating crack and an uncoated/coated elastic inclusion using BE technique. Int J Fract 114:47–61.
12. Kitey R, Phan AV, Tippur HV, Kaplan T (2006) Modeling of crack growth through particulate clusters in brittle matrix by symmetric-Galerkin boundary element method. Int J Fract 141(1):11–25.
13. Kitey R (2006) Microstructural effects on fracture behavior of particulate composites: investigation of toughening mechanism using optical and boundary element methods. Doctoral dissertation, Auburn University.
14. O'Toole BJ, Santare MH (1990) Photoelastic investigation of crack–inclusion interaction. Exp Mech 30(3):253–257.
15. Li R, Wu S, Ivanova E, Chudnovsky A, Sehaobish K, Bosnyak CP (1993) Finite element model and experimental analysis of crack–inclusion interaction. J Appl Polym Sci 50:1233–1238.
16. Post D, Baracat WA (1981) High-sensitivity moiré interferometry—a simplified approach. Exp Mech 21(3):100–104.
17. Post D, Han B, Ifju P (1994) High sensitivity moiré. Springer, Berlin Heidelberg New York.
18. Jaeger RC (2002) Introduction to microelectronic fabrication, vol 5, 2nd edn. Prentice-Hall, New Jersey.
19. Rousseau C-E, Tippur HV (2001) Influence of elastic gradient profiles on dynamically loaded functionally graded materials: cracks along the gradient. Int J Solids Struct 38:7839–7856.
20. Kirugulige MS, Kitey R, Tippur HV (2005) Dynamic fracture behavior of model sandwich structures with functionally graded core: a feasibility study. Compos Sci Technol 65:1052–1068.
21. ANSYS™ User's manual (Ver. 10). ANSYS Inc., Cannonsburg, PA.
22. Ko D, Kim B, Choi J (1997) Finite-element simulation of the shear process using the element-kill method. J Mater Process Technol 72:129–140.
23. Al-Ostaz A, Jasiuk I (1997) Crack initiation and propagation in materials with randomly distributed holes. Eng Fract Mech 58(5–6):95–420.

24. Xu XP, Needleman A (1994) Numerical simulation of fast crack growth in brittle solids. J Mech Phys Solids 42(9):1397–1434.
25. Xu XP, Needleman A (1995) Numerical simulations of dynamic interfacial crack growth allowing for crack growth away form the bond line. Int J Fract 74:253–275.
26. Madhusudhana KS, Narsimhan R (2002) Experimental and numerical investigations of mixed mode crack growth resistance of a ductile adhesive joint. Eng Fract Mech 69:865–883.
27. Abanto-Bueno J, Lambros J (2005) Experimental determination of cohesive failure properties of a photodegradable copolymer. Exp Mech 45(2):144–152.